Characterizing the performance of a POPS miniaturized optical particle counter when operated on a quadcopter drone

Zixia Liu[1], Martin Osborne[1,2], Karen Anderson[3], Jamie D. Shutler[3], Andy Wilson[2], Justin Langridge[2], Steve H.L. Yim[4,5,6,7], Hugh Coe[8], Suresh Babu[9], Sreedharan K. Satheesh[10], Paquita Zuidema[11], Tao Huang[4], Jack C.H. Cheng[4], Jim Haywood[1,2].

Affiliations:

[1]College of Engineering Mathematics, and Physical Sciences, University of Exeter, Exeter, Devon, UK

[2]Met Office, Fitzroy Road, Exeter, Devon, UK

[3]College of Life and Environmental Sciences, University of Exeter, Penryn, Cornwall, UK

[4]Department of Geography and Resource Management, The Chinese University of Hong Kong, Hong Kong, China

[5]Stanley Ho Big Data Decision Analytics Research Centre, The Chinese University of Hong Kong, Hong Kong, China

[6]Institute of Environment, Energy and Sustainability, The Chinese University of Hong Kong, Hong Kong, China

21 [7]Asian School of the Environment, Nanyang Technological University,

22 Singapore

23 [8]Department of Earth and Environmental Sciences, University of

24 Manchester, Manchester, UK

25 [9]Space Physics Laboratory, Vikram Sarabhai Space Centre, Trivandrum,

26 695 022, India

27 [10]Centre for Atmospheric and Oceanic Sciences, Indian Institute of Science,

28 Bangalore 560 012, India

29 [11]Rosenstiel School of Marine and Atmospheric Science, University of

30 Miami, Miami, FL, USA

31 *Correspondence to:* J. Haywood (J.M.Haywood@exeter.ac.uk)

32 **Abstract:**

33 We first validate the performance of the Portable Optical Particle Spectrometer (POPS),

34 a small light-weight and high sensitivity optical particle counter, against a reference

35 scanning mobility particle sizer (SMPS) for a month-long deployment in an

36 environment dominated by biomass burning aerosols. Subsequently, we examine any

37 biases introduced by operating the POPS on a quadcopter drone, a DJI Matrice 200 V2.

38 We report the root mean square difference (RMSD) and mean absolute difference

39 (MAD) in particle number concentrations (PNCs) when mounted on the UAV and

40 operating on the ground and when hovering at 10m. When windspeeds are low (less

41 than 2.6 m/s), we find only modest differences in the RMSDs and MADs of 5% and 3%

42 when operating at 10m altitude. When windspeeds are between 2.6 - 7.7m/s the RMSDs

43 and MADs increase to 26.2% and 19.1%, respectively when operating at 10m altitude.

44 No statistical difference in PNCs was detected when operating on the UAV in either

ascent or descent. We also find size distributions of aerosols in the accumulation mode (defined by diameter, d, where $0.1 \leq d \leq 1\mu m$) are relatively consistent between measurements at the surface and measurements at 10m altitude while differences in the coarse mode (here defined by $d > 1\mu m$) are universally larger. Our results suggest that the impact of the UAV rotors on the POPS PNCs are small at low windspeeds, but when operating under higher wind speed of up to 7.6m/s, larger discrepancies occur. In addition, it appears that the POPS measures sub-micron aerosol particles more accurately than super-micron aerosol particles when airborne on the UAV. These measurements lay the foundations for determining the magnitude of potential errors that might be introduced into measured aerosol particle size distributions and concentrations owing to the turbulence created by the rotors on the UAV.

1 Introduction

Atmospheric aerosols have a significant impact on Earth's climate as they affect the radiative balance of the Earth-Atmosphere system through the direct effect which refers to absorption and scattering of solar and terrestrial radiation, and the indirect effect which refers to the ability of aerosols to act as cloud condensation nuclei (CCN) (Haywood and Boucher, 2000; Boucher et al., 2013). Aerosol concentration and their intrinsic properties are spatially inhomogeneous owing to different emission sources, deposition processes, transports, and chemical reactions (e.g. Bellouin et al., 2005; Jiminez et al., 2009; Lack and Cappa, 2010; Atkinson et al., 2018; Yim et al., 2019; Yim et al., 2020).

67   Among these properties, particle size distributions (PSDs) and number concentrations

68   (PNCs) are of fundamental importance in determining the impact of aerosols on the

69   atmospheric radiation budget via the aerosol direct and indirect effects. Based on

70   observations of the size distributions of aerosols and aerosol refractive index, aerosol

71   optical properties can be inferred (e.g. Atkinson et al., 2015). The size of aerosol

72   particles is also of primary importance in cloud formation and precipitation (Yin et al.,

73   2000; Liu et al., 2018; 2019a). As a result, in order to better understand the effect of

74   aerosols on climate change, it is important to obtain a comprehensive and accurate

75   characterization of the spatial distribution of aerosol concentration and properties.

76   Aerosols can also impact atmospheric visibility (e.g. Horvath, 1981), air quality, and

77   health (e.g. Li et al., 2003; Gu et al., 2016; 2018; 2020; Shi et al., 2019). In terms of

78   scales, satellite observations (e.g. Bellouin et al., 2005) are able to provide near global

79   coverage of aerosol optical depths, but are only able to provide bulk measurements of

80   properties of the aerosol size distribution (e.g. fine mode fraction) and aerosol optical

81   properties (e.g. aerosol absorption). Dedicated field sites (e.g. Zuidema et al., 2016,

82   2018) or dedicated sampling with aircraft instrumentation (e.g. Haywood et al., 2003a;

83   2020) are able to make much more detailed aerosol microphysical measurements, but

84   are costly and aircraft cannot sample aerosols at low altitude in built-up urban regions

85   owing to obvious safety concerns.

86

87   The atmospheric science community frequently utilizes optical particle counters (OPCs)

88   and Mie scattering theory for sizing individual aerosol particles (e.g. Burkhart et al.,

89   2010). Measurements of aerosols by small, unmanned aerial vehicles (UAVs) have

90   many advantages, such as low-cost, ease and cost of deployment, and ease of access to

91   inaccessible areas such as those close to urban conurbations. However, owing to

92   payload restrictions, UAVs require light-weight, minaturized OPCs. The Portable

93   Optical Particle Spectrometer (POPS) is an advanced and small low-cost, light-weight,

94   and high-sensitivity OPC, particularly designed for UAVs and balloon sondes (Gao et

95   al., 2013; 2016). In brief, the POPS samples particles by drawing air through an inlet

96   tube into an optical chamber, where it is illuminated by a 405nm laser. A sheath air

97   flow is used to focus the sample air into the centre of the laser beam, and the sample

98   flow is maintained at a near constant rate by an automatically regulated on-board pump.

99   Individual particle sizes are then inferred by comparing the recorded signal amplitudes

100   to scattering amplitudes calculated using Mie scattering theory.

101

102   The POPS has been carried by balloon sondes to study the vertical profile of the Asian

103   Tropopause Aerosol Layer (Yu et al., 2017), but quantitative data when deployed on a

104   quadcopter drone is very sparse. There have been some recent side-by-side tests of

105   miniaturized OPC instruments against more established instrumentation in controlled

106   environments. For example, Bezantakos et al. (2018) compared a newly developed

107   miniaturized OPC against a GRIMM OPC across a range of atmospheric conditions.

108   There have also been some very limited comparisons of miniaturized UAV-borne OPC

instrumentation against measurements on large atmospheric tower based instrumentation (Ahn, 2019). Neither of these studies used a POPS OPC. Questions about the impact of inlets, and aircraft boundary layer depths on aerosol measurements have been the subject of research on aerosol for decades (Huebert et al., 1990; Sanchez-Marroquin, 2019). A similar significant question related to deploying the POPS instrument on a quadcopter drone is whether the turbulence generated by the multiple rotors and the attitude adjustment required to maintain positional stability impact the measurements of the aerosol concentrations and size distributions, and if so, to what extent. Here we provide the first comprehensive documentation of the performance of the POPS on a multi-rotor UAV. We first investigated the performance of the POPS instrument in a closely controlled environment on the ground in a three-week comparison of the POPS against reference instruments. The POPS was deployed at the Atmospheric Radiation Measurements (ARM) mobile facility on Ascension Island during colocation of the Layered Atlantic Smoke Interaction with Clouds (LASIC; Zuidema et al., 2016) and CLoud-Aerosol-Radiation Interaction and Forcing: Year-2017 (CLARIFY-2017; Haywood et al., 2020) measurement campaigns. Subsequently, when back in the UK, we examined the influence of the drone rotors and variability in the drone attitude on the measured aerosol number concentration and size distribution. Section 2 presents the methodology used in the ground-based comparison on Ascension Island. Section 2 also provides details of the methodology adopted for the UAV-mounted flights in UK. Section 3 presents the results before conclusions and future work is presented in section 4.

2 Methods

2.1 A 20-day comparison

As part of the CLARIFY-2017 and LASIC campaign, the POPS was deployed at the ARM mobile site on Ascension Island located in the mid-Atlantic (7.96° S, 14.37° W) alongside an ARM operated SMPS. The time period for sampling for both instruments analyzed here was from 20th August to 9th September 2017 (20 days) continuously, during which time biomass burning aerosol originating from the African continent was frequently present (Zuidema et al., 2018; Haywood, 2020). The SMPS and the POPS were connected to a common aerosol inlet, however, in the case of the SMPS, the sample air was dried before it entered the instrument.

In common with other OPCs, the POPS size distributions are influenced by the refractive index assumed in the Mie calculations. The manufacturer (Handix Scientific) provides a calibration for the POPS using well-sized latex spheres with a refractive index (RI) of 1.615+0.001i at 405 nm. Prior to deployment to Ascension Island, the manufacturer's calibration of the POPS was adjusted through independent lab-based measurements using latex spheres at the UK's Facility for Airborne Atmospheric Research (FAAM, https://www.faam.ac.uk/). Mie calculations were made for the specific geometry of the POPS sampling chamber and laser poarisation. The calibration procedure and associated Mie calculations are detailed in Appendix A. Errors in the PSDs can be caused by sampling aerosols with a different refractive index to that of latex, particularly if they are significantly absorbing (e.g. Haywood et al., 2003). The

153 independent lab-based calibration binning criteria were therefore adjusted assuming a

154 RI of 1.54+0.027i at 405 nm, which is expected to be more representative of the

155 biomass burning aerosol particles sampled at the ARM site during the CLARIFY

156 deployment (Peers et al., 2019). In contrast to the optical sizing nature of the POPS, the

157 SMPS that was operated by the ARM mobile Facility uses particle mobility subsequent

158 to application of an electrostatic charge to size aerosol particles, a method which is

159 independent of the refractive index (Ruzer and Harley, 2012).

160

161 In addition to applying fundamentally different methods to measure the size of particles,

162 the POPS and SMPS cover different ranges of size distributions. The POPS measures

163 particles within the diameter range from around $0.12 - 4.44\mu m$ (for RI = 1.54+0.027i

164 at 405 nm), while the SMPS covers diameter ranging from around 0.01 to $0.45\mu m$.

2.2 Drone-mounted POPS

166 The POPS required a carefully designed bespoke rig to fit it safely to a quadcopter

167 drone for deployment. A DJI Matrice 200 V2 was used because it had a sufficient power

168 and payload capacity to lift the POPS and even with the relatively high payload could

169 offer reasonable endurance. The maximum flight time of the Matrice is 24 minutes with

170 the maximum payload (1.45kg). University of Exeter and Met Office staff designed and

171 fitted the POPS to the Matrice airframe (Figure 1). The POPS was installed at the

172 bottom left of the fuselage and fixed on the customized 3-D printed landing gear. The

173 inlet tube of the POPS (red oval in Figure 1) reached 20cm above the rotors. The

174 diameter of the inlet tube is 1mm and the sample flow rate is 3 cm^3/s, yielding a flow

175 velocity of 3.8m/s. No attempt has been made to optimise this simple tube inlet for

176 drone applications. The data were collected during 14 test flights in total from 18th

177 December 2019 to 9th March 2020 to determine any impact of the rotors and attitude of

178 the UAV on the data from the POPS. Each test flight was planned to be separated into

179 three stages. During the first stage, the drone was on the ground with the rotors off for

180 ten minutes (G_NR). In the second stage, the drone was on the ground with the rotors

181 on for the next ten minutes (G_R). In the last stage the drone hovered at a fixed position

182 and fixed altitude of ten meters above the surface for ten minutes (FLY). A summary of

183 date and time of each test flight is given in Table 1. There are some deviations from the

184 G_NR, G_R and FLY routines. T1 was a pre-test so there was no FLY. Additionally,

185 due to high wind speeds and associated operational safety concerns, T9 and T13 had to

186 reduce the test time of FLY to 7 minutes and 5 minutes, respectively. Three vertical

187 profiles were made at the end of T10, T12, and T13, the details of which are provided

188 in the caption of Table 1. The main purpose of profiling during T10, T12 and T13 was

189 to investigate: 1) the stability in the POPS instrument when profiling up and down as

190 this is likely to be a prime operating maneuver when flying scientific sorties in the

191 future; 2) the performance of the POPS at different vertical ascent and descent rates;

192 and 3) the accuracy of the POPS on the way up and way down which could conceivably

193 be influenced by turbulent disturbance by the rotors, particularly on vertical descents

194 when the aerosol inlet will be in the wake of the drone rotors. The test flights were all

195 performed at the Streatham campus of the University of Exeter (50.73N, 3.53W), UK.

3 Results

3.1 Comparison of POPS data against data from LASIC/CLARIFY-2017.

Figure 2 shows the mean PSD measured by the POPS and SMPS for the 20-day period, respectively. Figure 2 represents the whole size range of the two instruments as well as the fitted PSD from measurements with a wing-mounted PCASP-100X mounted on the UK's Bae146 FAAM aircraft from a flight during CLARIFY-2017 (Peers et al., 2019), which has been shown to be representative of biomass burning aerosol during the wider CLARIFY-2017 measurement campaign (Wu et al., 2020). The POPS and SMPS were sampling at around 330m altitude ASL when at the LASIC site while the PCASP data from the CLARIFY campaign was collected from 1.9-7.3km ASL. That the POPS and SMPS show close overlap at the peak concentrations indicates that the counting statistics and the particle concentrations are similar between the instruments. The mean PSD measured by the POPS and SMPS shows reasonable agreement. Although the agreement is not as good as that demonstrated in other comparisons against SMPS instruments (e.g. Gao et al., 2016), any resulting errors in derived optical parameters are likely to be small provided the fit is reasonable over the 0.2-1.0 μm diameter range. Measurements of biomass burning aerosol over the Atlantic from the SAFARI-2000 campaign suggest that particles in this range contribute 93% of the scattering at 0.55μm (e.g. Table 1, Haywood et al., 2003). The PSD from the wing-borne PCASP-100X that was operated on the FAAM bears a close resemblance to the SMPS and POPS PSDs

217 except at particle sizes <0.2μm diameter and >0.7μm diameter. The discrepancy at

218 particle sizes <0.2μm might be expected because the fits that are adopted by Haywood

219 et al. (2003) and Peers et al. (2019) do not account for these small particles as they were

220 developed with simplicity in mind for global general circulation models and for satellite

221 retrievals respectively. Aerosols >0.7μm diameter that were observed by the POPS that

222 were not present in the CLARIFY-2017 or SAFARI-2000 data may well be generated

223 by dust generation from the arid surface of Ascension Island or by super-micron sea-

224 salt from breaking waves. Taylor et al (2020) document the enhanced influence of the

225 oceanic component of aerosols in the marine boundary layer, but this is not included in

226 the CLARIFY-2017 or SAFARI-2000 log-normal fits which represent biomass burning

227 aerosols only. Thus, the POPS instrument appears to provide a reasonably quantitative

228 measure of optically active sub-micron biomass burning aerosols.

229

230 We also investigated the overall particle number concentration from the POPS, and

231 examine the time series of the POPS measurements against some other key variables

232 measured by the SMPS and other instrumentation at the ARM mobile facility. The

233 upper panel of Figure 3a presents the 20-day intercomparison of the PNCs from the

234 POPS and SMPS, and panel 3b shows the ratio of the two concentration measurements

235 (POPS/SMPS). They show a good agreement between two instruments while the

236 geometric mean diameter (GMD) the of the size distribution (Figure 3c) is above

237 0.12μm. Again, this illustrates that the POPS instrument measures accumulation mode

238 aerosols reasonably accurately.

We would expect biomass burning aerosols to be associated with an increase in carbon monoxide (CO; Haywood et al., 2003; Wu et al., 2020), and the concentrations measured by both the POPS and SMPS instruments are well correlated with the CO volume mixing ratio (as measured by a co-located CO analyzer – Figure 3d). The concentration data also show some correlation with the AODs as measured by a co-located AERONET Cimel sun-photometer (panel five, Figure 3), although this AOD is a column measurement rather than a point measurement so the influence of vertical profile will likely be important (e.g. Wu et al, 2020; Haywood et al, 2020).

3.2 Test flight results

To determine the impact of rotors and drone attitude on the POPS, we focus on the comparison of PSD and PNC at three different stages: G_NR, G_R, and FLY. Table 1 summaries the mean PNC with standard deviation and the PNC percentage differences of each flight at different stages.

3.2.1. Particle number concentration (PNC)

Compared with the mean PNC at G_NR, the mean PNC at G_R changed from -1% to 26%, and that at FLY changed from -1% to 63%, respectively. However, it is apparent that the differences of PNCs are much lower in the cases T1, T2, T6, T7, and T10 (less than 10%) in both stages. Figure 4 shows the probability density functions of PNC in each case. A constant bin width is utilized across the G_NR, G_R, and FLY PDFs of each flight. Unpaired two-sample t-tests were selected to detect the similarity of the PNCs at different stages as the t-test is the most popular parametric test for samples

following normal distribution for calculating the significance of a small sample size

(De Winter, 2013). Here the PNC of G_NR was set as the control group, while that of

G_R and FLY was set as the perturbation groups using the mean PNC at each stage

every 30 seconds. Before the t-test, the Levene's test was performed which is an

inferential statistic used to assess the equality of variances for a variable calculated for

two or more groups (Levene, 1960). If the Levene's test cannot be passed, then the

unequal variances t-test, which is a more conservative test, was be applied for the

groups. The results (p value) of the t-test of each test flight are shown in Table 2.

For a significance level (α) set as 0.05, there are 5 test flights that passed the t test in

both G_R and FLY stages (p value $\geq \alpha$), which means the PNC measured at G_R and

FLY stage corresponded well with those measured at G_NR. These test numbers have

been marked in bold italic font in Table 2. This result indicates that the impact of rotors

and UAV attitude was not significant in these five cases. The other three cases (T8, T9,

and T14) passed the t-test in the G_R stage, which are marked in italic font. The rest of

test flights did not pass the t-test in either stage (marked in standard font). Through

comparing the weather conditions, we find that the wind speed (Table 2) was relatively

lower (0.5-2.6m/s) in the cases which pass the t-test at both stages. The wind speed in

the Table 2 was provided from observations at Exeter airport with one-hour resolution.

During the actual experiment, when the wind speed was high, visual observations by

the drone pilot suggested that the drone swung from side to side in the air, causing

increased variability in the pitch, yaw and altitude of the drone. As previously noted,

on T9 and T13 the drone was forced to land early to ensure safety due to the high (>7

283   m/s) instantaneous wind speed.

284

285   To determine the impact of wind speed on PNC observed by the POPS, the cases are

286   separated into 2 categories: low wind speed (w<2.6m/s) cases and high wind speed

287   (2.6<w<7.7m/s) cases. The PNC root mean square differences (RMSD) and mean

288   absolute differences (MAD) at G_R and FLY for all cases, low wind speed cases, and

289   high wind speed cases are given in the Table 3. For all cases, PNC RMSD is less than

290   10.2% at G_R and less than 26.2% at FLY, and MAD is less than 7.8% at G_R and less

291   than 19.1% at FLY. However, in the low wind cases, the RMSD and MAD fall to 2.4%

292   and 2.3% at G_R, and 5% and 3% at FLY, respectively. In contrast, RMSD and MAD

293   in the high wind cases increase to 12.6% and 10.9% at G_R, 31.4% and 26.3% at FLY,

294   respectively. The variability in the pitch, yaw and altitude of the drone also impacted

295   the orientation of the inlet of the POPS, which ideally should be perpendicular to the

296   horizontal plane. Variations in the orientation of the inlet led to increased scatter in the

297   sample flow rate. Table 4 shows mean sample flow rates with standard deviation at

298   G_NR, G_R, and FLY for all cases. It is clear that for G_NR, the mean flow rates were

299   constant across all tests and the standard deviation in the flow rates were very low.

300   Comparing with G_NR, the mean sample flow rate and the standard deviation were

301   almost unchanged with for G_R. This shows that operating the rotors alone didn't

302   impact the sample flow rate. However, while the mean flow rate during FLY was

303   identical to G_NR, the standard deviations increased during the FLY stage, particularly

304   for the tests under high windspeeds. The mean value of the standard deviation for low

305 windspeed cases was 0.13, while for the high windspeed cases was 0.21 which may

306 influence the accuracy of the POPS measurements.

307

308 3.2.2. The particle size distribution (PSD)

309 The PSDs at different stages and the mean PSDs ratios at G_R to G_NR and FLY to

310 G_NR of each test flight are shown in Figure 5, which indicates that the cases with high

311 similarity of PNCs (T1, T2, T6, T7, and T10) show agreement of the PSD. It also shows

312 that the differences in sub-micron sizes are less than those in super-micron sizes at G_R

313 and FLY. Therefore, the size distribution was separated into two modes, the

314 accumulation mode ($0.1 \leq d \leq 1.0\mu m$) and the coarse mode ($d > 1.0\mu m$), to make a

315 statistical analysis. Table 5 summarizes the PSDs percentage differences for two modes

316 at G_R and FLY for each case. The PSDs RMSD and MAD for two modes at G_R and

317 FLY for all cases, low wind cases, and high wind cases are given in Table 5. The

318 percentage differences of the PSDs are less than 5.4% and 14.9% in low wind cases at

319 the accumulation mode at G_R and FLY, respectively, while the variation in the PSD in

320 the coarse mode is perhaps due to lower counting statistics at these sizes. In contrast

321 PSDs of other cases show differences across the whole spectrum. Even in the

322 accumulation mode, the differences of the PSDs between FLY and G_NR are up to 53.2%

323 in the case T8. PSDs RMSD and MAD at the accumulation mode are 3.4% and 2.7%

324 respectively at G_R in the low wind speed cases, but up to 12.9% and 11.1% at G_R in

325 the high wind speed cases. These statistics again indicate that impacts of rotors and

326 UAV attitude on the POPS measurements appear to be reduced in low wind speeds

327 relative to higher wind speeds. PSD RMSDs and MADs at the coarse mode at G_R,

328 and at the accumulation and coarse mode at FLY show the same result. Generally

329 speaking, RMSDs and MADs indicate the impact of rotors and UAV attitude on the

330 performance of the POPS in measuring the accumulation mode is lower than in

331 measuring the coarse mode, for all cases. RMSDs in accumulation mode were 10.6%

332 at G_R and 21.6% at FLY, while those in coarse mode were 32.2% and 49.5% for all

333 cases. MADs showed the same trend as RMSDs. In the absence of independent multi-

334 stage meteorological tower measurements (e.g. Ahn, 2019), it is difficult to assess how

335 much of the variability in PNCs and PSDs is real, particularly when the drone is flying;

336 there may be changes in PNC with altitude when compared to the surface PNCs owing

337 to surface deposition. Alternatively, there may be trends in the particle concentrations

338 that occur during the entire measurement period which spanned around 30 minutes

339 duration. We determine trends in the G_NR and G_R statistics by determining the mean

340 slope (particles / s) during the operating periods; only flights T4 and T6 show trends of

341 greater than 0.1 particles per second (6 particles / minute) when averaged over both

342 G_NR and G_R. Figure 4 shows that there is potentially an increase in the

343 concentrations that are measured during T4, and that there is potentially a bi-modal

344 number concentration measured during the G_NR sampling period for T6. As no trends

345 are evident for the other flights, it can be inferred that there is no evidence of a

346 systematic significant trend in atmospheric concentrations across all flights; any such

347 trends are likely to be random. However, a potential solution to any concern would be

348 to change the three stage sequence from G_NR, G_R, FLY to a five stage sequence of

349   G_NR, G_R, FLY, G_R and G_NR. This sequence is suggested for future investigations.

350

351   3.2.3. The PNC during vertical profiles

352   Figure 6 presents the results of the vertical profile runs in T10, T12, and T13. The mean

353   PNC with standard deviation on the way up and down are shown in Table 6. The PNC

354   measured on the way up and way down show agreement. The best agreement is found

355   in the high number concentration, low wind-speed case (T10), where the PNCs differ

356   by an average of 0.5% between ascent and descent. Even in the high wind-speed cases

357   when the variability might be expected to be largest owing to changes in the pitch and

358   yaw of the drone, general agreement is found indicating that the vertical speed of the

359   drone (which was approximately 0.5 to 1m/s) does not appear to have a significant

360   impact. Note that the vertical profiles do indicate some variability in the vertical

361   distribution with PNCs ranging from 1207 ± 83 cm^{-3}, 69 ± 14 cm^{-3}, and 90 ± 11 cm^{-3} close to

362   the surface to 1189 ± 107 cm^{-3}, 55 ± 11 cm^{-3}, and 72 ± 15 cm^{-3} in ascent and 1395 ± 83 cm^{-3},

363   69 ± 5 cm^{-3}, and 89 ± 6 cm^{-3} close to the surface to 1201 ± 101 cm^{-3}, 54 ± 12 cm^{-3}, and 82 ± 13

364   cm^{-3} in descent for flights T10, T12 and T13. The close to surface data were collected

365   by the UAV-mounted POPS when the drone was 1-3 meters above the surface. This

366   variability with height emphasizes the utility of small, instrumented UAVs for

367   measuring PNCs and PSDs at low altitudes; measurements at such altitudes are

368   impossible to probe with heavily equipped atmospheric research aircraft operating

369   under standard aviation safety protocols.

4 Discussion and conclusions

We have investigated the performance of POPS against a reference SMPS instrument while on the ground and also while operated on a quadcopter drone, DJI Matrice 200 V2, which is the first documented test of the performance of a POPS instrument on a UAV. The investigation includes two parts. The first is a long-term comparison between the POPS and other instruments during the CLARIFY-2017/LASIC and SAFARI-2000 project. The results show that the PNC measured by the POPS and that measured by the SMPS and PCASP indicate agreement in the optically important size range centred at around 0.3μm diameter. This indicates that despite its small size, when operating under controlled conditions on the ground, the POPS instrument performs relatively well. In the second part, we tested the impact of drone's rotors and, indirectly the attitude of the drone, on the performance of the POPS with a focus on two aspects, the PNC and PSD. We found RMSDs and MADs in PNC when operating a POPS on a small quad-copter to be less than 10.2% and 7.8%, respectively, when operating on the ground, and less than 26.2% and 19.1%, respectively, at 10m altitude under wind speed conditions of up to 7.7m/s. For wind speed of less than 2.6m/s, RMSDs and MADs fell to 2.4% and 2.3% when operating on the ground, and to 5% and 3% at 10m altitude. We also found no statistical difference in PNC when operating the UAV in either ascent or descent. As for the PSD, the accumulation mode aerosol size distributions were relatively invariant between measurements at the surface and measurements at 10m altitude with RMSD and MAD of less than 21.6% and 15.7%, respectively. The

391 differences between coarse mode super-micron aerosols measured at the surface and at

392 10m altitude were universally greater than those measured at the surface with a RMSD

393 and MAD approaching 49.5% and 40.4%, but it is unclear whether this is due to loss

394 of coarse mode aerosol particles to the surface or whether this is due to interference

395 from the rotors. This impact appears to be most prevalent at the larger end of the POPS

396 size range. While the increase in PNC from G_NR to G_R might be explained by

397 generation or resuspension of aerosols from the surface by the rotors of the UAV, the

398 increase from G_R to FLY is more difficult to attribute. The surface acts as a net sink

399 in aerosols through dry deposition which could lead to an increase in PNC with altitude

400 (e.g. Pellerin et al., 2017), but there are confounding factors from changes in the attitude

401 of the drone and rapid changes in the attitude necessary for stabilizing the position of

402 the UAV during FLY that could also influence the measurements. Indeed, there is

403 evidence that fast adjustments to the attitude of the UAV increase the variability in the

404 flow rate reported by the POPS sensor, particularly at higher windspeeds, where these

405 corrections are larger. These results suggest that, when the wind-speed is modest, the

406 POPS and UAV and very simple inlet combination examined here appears able to

407 measure the aerosol PSD and PNC with reasonable fidelity, particularly for sub-micron

408 aerosols.

409

410 In follow-up scientific observations, the POPS deployed on the quadcopter drone will

411 be used to measure the aerosol properties in the atmospheric boundary layer (ABL)

412 under polluted condition. Concentration of pollutants in the ABL frequently have a

strong correlation with atmospheric stability (Wang et al., 2013, Chambers et al., 2015)

with stable conditions leading to the build-up of pollutants in the ABL. Wind-speeds

are frequently low in stable conditions due to the lack of convection driven turbulence.

Because these future measurements are likely under stable, non-turbulent conditions,

wind-speed effects are not likely to cause significant problems. For other applications

of the POPS on a quadcopter drone, such as the dispersion of pollutants in down-wind

driven plumes, attention should be paid to the influence of the higher wind speeds.

Appendix A

POPS calibration

The calibration procedure used to adjust the POPS size bins for refractive index

followed the general OPC calibration methodology described in Rosenberg et al. 2012

and Gao et al. 2016. By sampling a series of mono-disperse particles of known

refractive index we compared the scattering amplitudes measured by the POPS to

scattering amplitudes calculated using Mie theory.   Scaling the Mie calculated

amplitudes to match the measured scattering amplitudes results in a scaling factor that

accounts for the POPS laser energy and detector efficiency.   The scaling factor can

then be used to convert Mie calculated scattering amplitudes for any refractive index to

the arbitrary units of the POPS.

Calibration measurements

The calibration used NIST traceable polystyrene latex (PSL) spheres in 22 sizes,

433   ranging from 0.147μm to 3μm. The manufacturer's stated refractive index is 1.615-

434   0.001i. An air source and a nebuliser cup were connected via rubber tubing to the POPS

435   inlet and a few minutes of data collected for each of the 22 sizes of PSL sphere. The

436   result was a histogram of POPS digitizer values for each size. We fitted normal

437   distributions to these and took the mode and standard deviation as the POPS scattering

438   value and associated error.

Polarised Mie scattering calculations for the POPS geometry

440   The Mie scattering calculations were made using the miepython library available from

441   https://pypi.org/project/miepython/. We calculated POPS specific scattering amplitudes

442   for spherical particles by integrating the scattering phase functions over only the POPS

443   collection angles. Gao et al. 2016 describes the geometry of the POPS detection

444   chamber and this is shown in Figure A1.

445   According to Bohren and Huffman 1983, for a homogeneous spherical particle

446   illuminated by an electromagnetic plane wave $E_i = E_{\parallel i} + E_{\perp i}$, the scattered wave

447    $E_s = E_{\parallel s} + E_{\perp s}$ as observed a constant distance from the particle can be written as:

448

449
$$\begin{bmatrix} E_{\parallel s} \\ E_{\perp s} \end{bmatrix} = constant \begin{bmatrix} S_2 & 0 \\ 0 & S_1 \end{bmatrix} \begin{bmatrix} E_{\parallel i} \\ E_{\perp i} \end{bmatrix} \tag{A1}$$

450

451   Where $E_{\parallel} + E_{\perp}$ are the components of the electric fields parallel and perpendicular to

452   the scattering plane, and S_1 and S_2 are elements of the amplitude scattering matrix

453   describing the angular distribution of the scattered light. According to Gao et al. 2016

454   the POPS laser diode is oriented such that the plane of polarisation of the laser is

455   perpendicular to the scattering plane (so perpendicular to the plane of the page in fig.

456   1), and so $E_{\parallel i}$ = zero. As the diagonal elements of the amplitude scattering matrix are

457   zero, $E_{\parallel s}$ is also zero, meaning that the scattered field contains no component parallel

458   to the scattering plane. Therefore, the scattering amplitude for the POPS, σ_{pops}, is

459   given by:

460

461    $\sigma_{pops} = \frac{\pi D_p{}^2}{8} Q_{sca} \int_0^{2\pi} \int_0^{\pi} (|S_1|^2)\, F_{pops}(\theta, \varphi) \sin\theta\, d\theta d\varphi$ (A2)

462

463   Where θ and φ are the zenith and azimuthal scattering angles respectively (we

464   measure φ from horizontal - that is downwards from the plane perpendicular to the

465   page in Figure A1). D_p is particle diameter, Q_{sca} is the Mie scattering efficiency

466   factor and F_{pops} is a weighting function that accounts for the collection angles of the

467   POPS. To construct the weighting function F_{pops} we find the combinations of θ and

468   φ for which the phase function hits the collection mirror (F_{pops} = 1) and when it is

469   outside of the mirror (F_{pops}= 0). From Figure A1 and the information given in Table

470   A1, for 38°≤θ ≤142° and $\varphi = \pi/2$, the scattered beam hits the collection mirror a

471   vertical distance q from the axis of the incident beam given by:

472    $q = R\, \cos(90 - \theta)$ (A3)

473   where

474    $R = \frac{l_d \sin((90 - \theta) - \alpha)}{\sin(90 + \theta)}$ (A4)

475   and

476 $\alpha = \sin^{-1}\left(\frac{(I_d - d)\sin(90 + \theta)}{I_d}\right)$ (A5)

477 and using the lens equation

478 $I_d = \frac{1}{\left[\frac{1}{f_m} - \frac{1}{d}\right]}$ (A6)

479 For a given value of θ, as the azimuthal angle φ rotates away from $\pi/2$, the distance

480 q will shorten by a factor of cos (90 - φ), and when q is less than the distance h (the

481 distance from the beam to the horizon of the mirror) the scattered beam will no longer

482 hit the mirror. So finally, for 38º≤θ ≤142º we have:

483 F_{pops} = 1 where q cos (90 - φ) > h ; else F_{pops} = 0 (A7)

Results

485 The blue curve in Figure A2 is the result of using equations A1 and A7 and a refractive

486 index of 1.615-0.001i for particle diameters 0.1μm to 4μm (as a sanity check, this curve

487 is nearly identical in shape to that shown in Figure 6 of Gao et al. 2016). The scattering

488 amplitudes measured during the calibration using PSL spheres are plotted in red. The

489 vertical error bars are one standard deviation of the normal distribution. The Mie

490 scattering curve has been scaled (using a least squares fit) to match the scattering

491 amplitudes measured during the calibration using.

492 The black curve in Figure A2 is the result of using a biomass burning like refractive

493 index of 1.54-0.27i in the Mie calculations. This curve has also been scaled using the

494 same factor as the blue PSL sphere curve.

Bin boundaries for biomass burning like particles

For particle sizing, we used 16 bins logarithmically spaced along the scattering amplitude axis. We then used a monotonic fit to the scaled scattering amplitude curve for biomass burning to relate these bin boundaries to particle diameters, giving the bin boundaries as shown in Figure A3.

Acknowledgements: This work was supported by the Chinese University of Hong Kong – University of Exeter Joint Centre for ENvironmental SUstainability and REsilience (ENSURE) programme; ZL, MO, JH, KA, JS, TH, JC and SY would like to thank ENSURE for their financial support. JH, ZL and HC would also like to acknowledge NERC SWAAMI (South West Asian Aerosol Monsoon Interactions) grants NE/L013878/1 and NE/L013886/1 NERC CLARIFY-2017 Large Grant NE/L013584/1 for partial funding of the research.

References

Ahn, K-H, Aerosol 3D Profiling Using Compact Particle Measuring Instruments with Balloon and Drone System, *7th International Symposium on Ultrafine Particles, Air Quality and Climate (2019)*, DOI: 10.5445/IR/1000096749,

Albrecht, B. A. (1989). Aerosols, cloud microphysics, and fractional cloudiness. *Science*, *245*(4923), 1227-1230.

Atkinson, D. B., Pekour, M., Chand, D., Radney, J. G., Kolesar, K. R., Zhang, Q., Setyan, A., O'neill, N. T. & Cappa, C. D. 2018. Using spectral methods to obtain particle size information from optical data: applications to measurements from CARES 2010. Atmospheric Chemistry and Physics, 18, 5499-5514.

Atkinson, D. B., Radney, J. G., Lum, J., Kolesar, K. R., Cziczo, D. J., Pekour, M., Zhang, Q., Setyan, A., Zelenyuk, A. & Cappa, C. D. 2015. Aerosol optical hygroscopicity measurements during the 2010 CARES campaign. Atmospheric Chemistry and Physics, 15, 4045–4061.

Bezantakos, S., Schmidt-Ott, F., Biskos, G., 2018. Performance evaluation of the cost-effective and lightweight Alphasense optical particle counter for use onboard unmanned aerial vehicles. Aerosol Sci. Technol. 52, 385–392.

Bellouin, N., Boucher, O., Haywood, J., & Reddy, M. S. (2005). Global estimate of aerosol direct radiative forcing from satellite measurements. Nature, 438(7071), 1138-1141.

Boucher, O., D. Randall, P. Artaxo, C. Bretherton, G. Feingold, P. Forster, V.-M. Kerminen, Y. Kondo, H. Liao, U. Lohmann, P. Rasch, S.K. Satheesh, S. Sherwood, B. Stevens and X.Y. Zhang, 2013: Clouds and Aerosols. In: Climate Change 2013: The Physical Science Basis. Contribution of Working Group I to the Fifth Assessment Report of the Intergovernmental Panel on Climate Change [Stocker, T.F., D. Qin, G.-K. Plattner, M. Tignor, S.K. Allen, J. Boschung, A. Nauels, Y. Xia, V. Bex and P.M. Midgley (eds.)]. Cambridge University Press, Cambridge, United Kingdom and New York, NY, USA.

Burkart, J., Steiner, G., Reischl, G., Moshammer, H., Neuberger, M., & Hitzenberger, R. (2010). Characterizing the performance of two optical particle counters (Grimm OPC1. 108 and OPC1. 109) under urban aerosol conditions. Journal of Aerosol Science, 41(10), 953-962.

Chambers, S. D., Wang, F., Williams, A. G., Xiaodong, D., Zhang, H., Lonati, G., Crawford, J., Griffiths, A. D., Ianniello, A. & Allegrini, I. 2015. Quantifying the influences of atmospheric stability on air pollution in Lanzhou, China, using a radon-based stability monitor. Atmospheric Environment, 107, 233-243.

De Winter, J. C. 2013. Using the Student's t-test with extremely small sample sizes. Practical Assessment, Research, and Evaluation, 18, 10.

Gao, R., Perring, A., Thornberry, T., Rollins, A., Schwarz, J., Ciciora, S. & Fahey, D. 2013. A high-sensitivity low-cost optical particle counter design. Aerosol Science and Technology, 47, 137-145.

Gao, R., Telg, H., Mclaughlin, R., Ciciora, S., Watts, L., Richardson, M., Schwarz, J., Perring, A., Thornberry, T. & Rollins, A. 2016. A light-weight, high-sensitivity particle spectrometer for PM2. 5 aerosol measurements. Aerosol Science and Technology, 50, 88-99.

Gu Y. and Yim S.H.L. (2016). The air quality and health impacts of domestic trans-boundary pollution in various regions of China. Environment International, 97, 117-124.

Gu Y., Wong T.W., Law S.C.K., Dong G.H., Ho K.F., Yang Y., Yim S.H.L. (2018). Impacts of Sectoral Emissions in China and the Implications: Air Quality, Public Health, Crop Production, and Economic Costs. Environmental Research Letters, 13, 8.

Gu Y., Zhang W., Yang Y., Wang C., Streets D.G., Yim S.H.L. (2020). Assessing outdoor air quality and public health impact attributable to residential black carbon emissions in rural China. Resources, Conservation and Recycling, 159, 104812.

Haywood, J., & Boucher, O. (2000). Estimates of the direct and indirect radiative forcing due to tropospheric aerosols: A review. Reviews of geophysics, 38(4), 513-543.

Haywood, J., Francis, P., Dubovik, O., Glew, M. & Holben, B. 2003a. Comparison of aerosol size distributions, radiative properties, and optical depths determined by aircraft observations and Sun photometers during SAFARI 2000. Journal of Geophysical Research: Atmospheres, 108.

Haywood, J. M., Osborne, S. R., Francis, P. N., Keil, A., Formenti, P., Andreae, M. O. & Kaye, P. H. 2003b. The mean physical and optical properties of regional haze dominated by biomass burning aerosol measured from the C-130 aircraft during SAFARI 2000. Journal of Geophysical Research: Atmospheres, 108.

Haywood, J.M., S. J. Abel, P. Barrett, N. Bellouin, A. Blyth, K.N. Bower, M. Brooks, K. Carslaw, H. Coe, M. Cotterell, I. Crawford, N. Davies, B. Dingley, P. Field, P. Formenti, H. Gordon, M. de Graaf, R. Herbert, B. Johnson, A.C. Jones, F. Malavelle, D.G. Partridge, F. Peers, J. Redemann, P. Stier, J. Taylor, R. Wood, H.H. Wu, P. Zuidema. Overview of the CLoud-Aerosol-Radiation Interaction and Forcing: Year-2017 (CLARIFY-2017) measurement campaign, acp-2020-729, Atmos Chem Phys Diss, 2020.

Horvath, H. (1981). Atmospheric visibility. Atmospheric Environment (1967), 15(10-11), 1785-1796.

Huebert, B. J., Lee, G., & Warren, W. L. (1990). Airborne aerosol inlet passing efficiency measurement. Journal of Geophysical Research: Atmospheres, 95(D10), 16369-16381.

IPCC: Climate Change 2013: The Physical Science Basis. Contri- bution of Working Group I to the Fifth Assessment Report of the Intergovernmental Panel on Climate Change, Cambridge University Press, Cambridge, United Kingdom and New York, NY, USA, 2013.

Jimenez, J.L., Canagaratna, M.R., Donahue, N.M., Prevot, A.S.H., Zhang, Q., Kroll, J.H., DeCarlo, P.F., Allan, J.D., Coe, H., Ng, N.L. and Aiken, A.C., 2009. Evolution of organic aerosols in the atmosphere. Science, 326(5959), pp.1525-1529.

Lack, D. & Cappa, C. 2010. Impact of brown and clear carbon on light absorption enhancement, single scatter albedo and absorption wavelength dependence of black carbon. Atmospheric Chemistry and Physics, 10, 4207.

Levene, H. 1960. Robust tests for equality of variances. Ingram Olkin, Harold Hotelling, et alia. Contributions to Probability and Statistics: Essays in Honor of Harold Hotelling. Stanford University, 278-292.

Li, N. Hao, M. Phalen, R. Hinds, W. and Nel, N. "Particulate air pollutants and asthma: a paradigm for the role of oxidative stress in PM-induced adverse health effects." Clinical immunology 109, no. 3 (2003): 250-265.

Liu Z., Ming Y., Zhao C., Lau N.C., Guo J., Bollasina M., Yim S.H.L. (2019a). Contribution of local and remote anthropogenic aerosols to a record-breaking torrential rainfall event in Guangdong Province, China. Atmospheric Chemistry and Physics, 20, 223-241.

Liu Z., Ming Y., Wang L., Bollasina M., Luo M., Lau N.C., Yim S.H.L. (2019b). A Model Investigation of Aerosol-Induced Changes in the East Asian Winter Monsoon. Geophysical Research Letters, 46(16), 10186-10195.

Liu Z., Yim S.H.L., Wang C., Lau N.C. (2018). The impact of the aerosol direct radiative forcing on deep convection and air quality in the Pearl River Delta region. *Geophysical Research Letters*, 45(9), 4410-4418.

Peers, F., Francis, P., Fox, C., Abel, S.J., Szpek, K., Cotterell, M.I., Davies, N.W., Langridge, J.M., Meyer, K.G., Platnick, S.E. and Haywood, J.M., 2019. Observation of absorbing aerosols above clouds over the south-east Atlantic Ocean from the geostationary satellite SEVIRI–Part 1: Method description and sensitivity. *Atmospheric Chemistry and Physics*, 19, 9595–9611, 2019 https://doi.org/10.5194/acp-19-9595-2019.

Pellerin, G., Maro, D., Damay, P., Gehin, E., Connan, O., Laguionie, P., Hébert, D., Solier, L., Boulaud, D., Lamaud, E. and Charrier, X., 2017. Aerosol particle dry deposition velocity above natural surfaces: quantification according to the particles diameter. Journal of Aerosol Science, 114, pp.107-117.

Ruzer, L. S. & Harley, N. H. 2012. Aerosols handbook: measurement, dosimetry, and health effects, CRC press.

Sang-Nourpour, N., & Olfert, J. S. (2019). Calibration of optical particle counters with an aerodynamic aerosol classifier. *Journal of Aerosol Science*, 138, 105452.

Sanchez-Marroquin, A., Hedges, D. H. P., Hiscock, M., Parker, S. T., Rosenberg, P. D., Trembath, J., Walshaw, R., Burke, I. T., McQuaid, J. B., and Murray, B. J.: Characterisation of the filter inlet system on the FAAM BAe-146 research aircraft and its use for size-resolved aerosol composition measurements, Atmos. Meas. Tech., 12, 5741–5763, https://doi.org/10.5194/amt-12-5741-2019, 2019.

Shi C., Nduka I.C., Yang Y., Huang Y., Yao R., Zhang H., He B., Xie C., Wang Z., Yim S.H.L. (2019). Characteristics and Meteorological Mechanisms of Transboundary Air Pollution in A Persistent Heavy PM2.5 Pollution Episode in Central-East China. *Atmospheric Environment*, 223, 117239.

Taylor, J. W., Wu, H., Szpek, K., Bower, K., Crawford, I., Flynn, M. J., Williams, P. I., Dorsey, J., Langridge, J. M., Cotterell, M. I., Fox, C., Davies, N. W., Haywood, J. M., and Coe, H.: Absorption closure in highly aged biomass burning smoke, *Atmospheric Chemistry and Physics*, 20, 11201–11221, https://doi.org/10.5194/acp-20-11201-2020, 2020.

Twomey, S. (1977). The influence of pollution on the shortwave albedo of clouds. *Journal of the atmospheric sciences*, 34(7), 1149-1152.

Wang, F., Zang, H., Ancora, M. & Deng, X. 2013. Measurement of atmospheric stability index by monitoring radon natural radioactivity. *China Environmental Science*, 33, 594-598.

Wu, H.,   J.W. Taylor, K. Szpek, P.I. Williams, M. Flynn, J. Langridge, J.D. Allan, J. Pitt, S. Abel, J. Haywood, H. Coe, Vertical and temporal variability of the properties of transported biomass burning aerosol over the southeast Atlantic during CLARIFY-2017, *ACPD.*.

Yim S.H.L., Gu Y., Shapiro M., Stephens B. (2019). Air quality and acid deposition impacts of local emissions and transboundary air pollution in Japan and South Korea. *Atmospheric*

Chemistry and Physics, 19, 13309-13323.

Yim S.H.L. (2020). Development of a 3D Real-Time Atmospheric Monitoring System (3DREAMS) Using Doppler LiDARs and Applications for Long-Term Analysis and Hot-and-Polluted Episodes. *Remote Sensing* 12 (6), 1036.

Yin, Y., Levin, Z., Reisin, T. G. & Tzivion, S. 2000. The effects of giant cloud condensation nuclei on the development of precipitation in convective clouds—A numerical study. *Atmospheric Research*, 53, 91-116.

Yu, P., Rosenlof, K. H., Liu, S., Telg, H., Thornberry, T. D., Rollins, A. W., Portmann, R. W., Bai, Z., Ray, E. A. & Duan, Y. 2017. Efficient transport of tropospheric aerosol into the stratosphere via the Asian summer monsoon anticyclone. *Proceedings of the National Academy of Sciences*, 114, 6972-6977.

Zuidema, P., Sedlacek III, A.J., Flynn, C., Springston, S., Delgadillo, R., Zhang, J., Aiken, A.C., Koontz, A. and Muradyan, P., 2018. The Ascension Island boundary layer in the remote southeast Atlantic is often smoky. *Geophysical Research Letters*, 45(9), pp.4456-4465.

Zuidema, P., Redemann, J., Haywood, J., Wood, R., Piketh, S., Hipondoka, M. and Formenti, P., 2016. Smoke and clouds above the southeast Atlantic: Upcoming field campaigns probe absorbing aerosol's impact on climate. *Bulletin of the American Meteorological Society*, 97(7), pp.1131-1135.

Figure 1. The DJI Matrice 200 V2 with the POPS (white box at the left bottom of the fuselage). The red oval shows the inlet tube leading to the POPS.
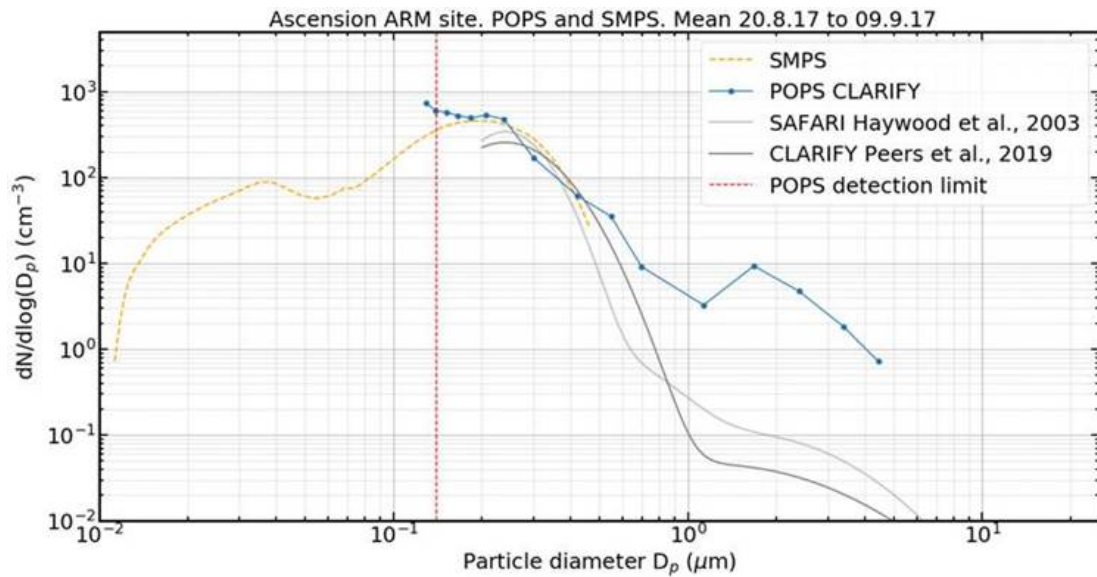
Figure 2. PSDs from POPS, SMPS, and data fitted to a wing-mounted PCASP from CLARIFY-2017 and SAFARI-2000. POPS and SMPS data were collected at the ARM mobile site on Ascension Island from 20th of August to 9th of September 2017.The PCASP data from CLARIFY were collected from a flight on 4th of September 2017 (Peers et al., 2019). The PCASP data from SAFARI-2000 represent a mean from 11 flights performed off the coast of Namibia (Haywood et al., 2003). Note that the CLARIFY-210 and SAFARAI-2000 PCASP distributions are 'scaled' to the SMPS size distribution to aid comparison. The POPS and SMPS values are not scaled.   ·

705
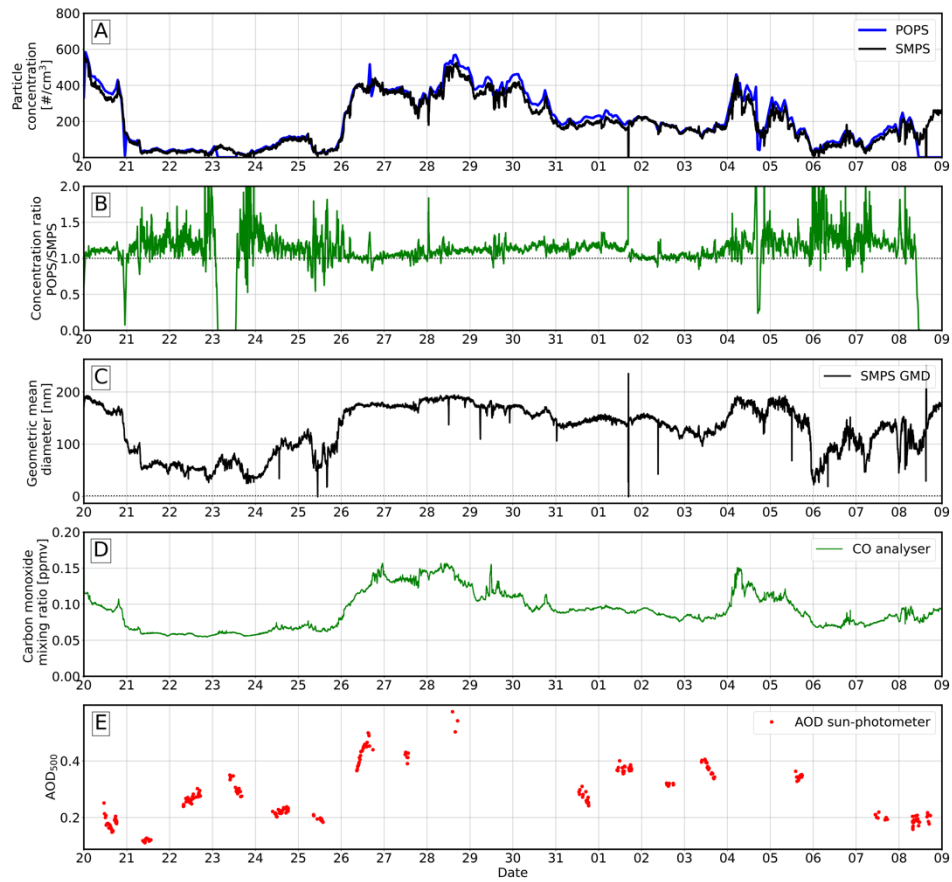
706 **Figure 3.** From top to bottom. (a) Time series of SMPS and POPS particle concentrations in the
707 diameter range 120 – 450 nm measured during the LASIC/CLARIFY-2017 campaign. (b) Ratio of
708 the POPS to SMPS concentrations shown in (a). (c) Geometric mean diameter from SMPS. (d)
709 Carbon monoxide mixing ratio from Los Gatos Research CO analyser, and (e) AOD from Cimel
710 sun- photometer.

711
712
713
714
715
716

717
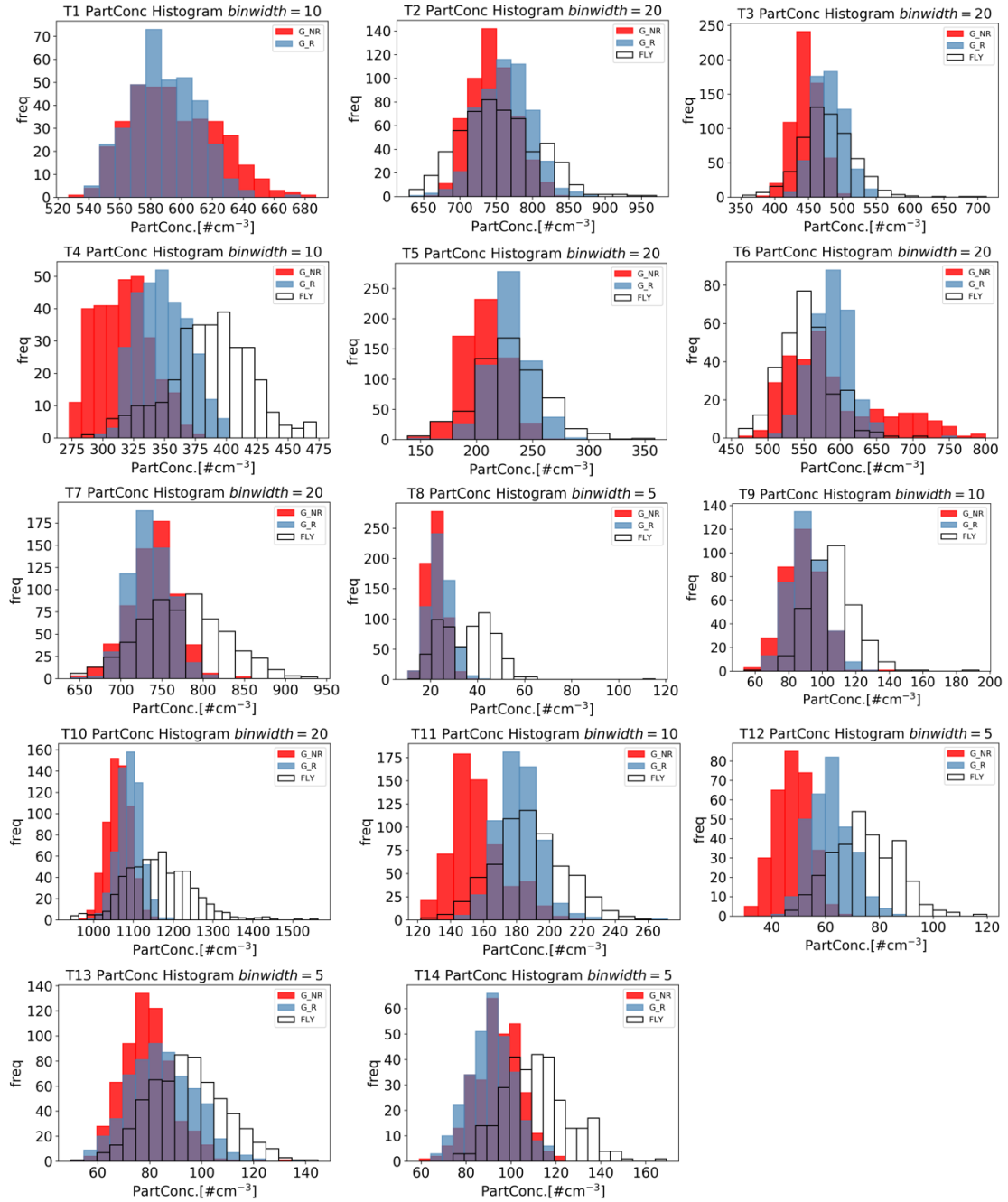
Figure 4. Probability density functions (PDFs) of PNCs in each case. A constant bin width is utilized across the G_NR, G_R, and FLY PDFs of each flight.

718
719
720
721
722
723
724
725
726
727

728
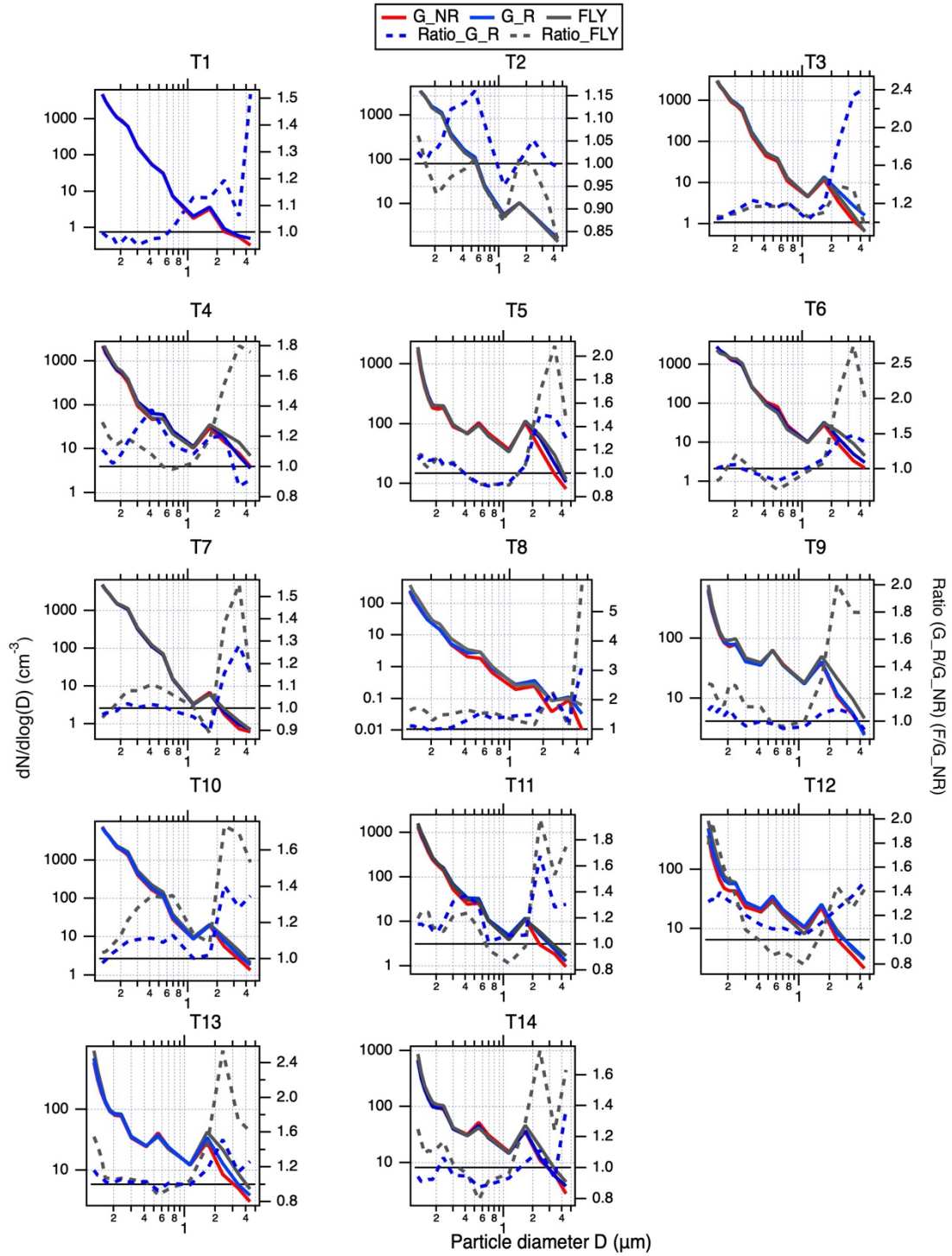
Figure 5. Particle size distribution at three stages: the drone on the ground with rotors off (G_NR) (red line), on the ground with rotors on (G_R) (blue line) and flying at 10m (FLY) (grey line), in each POPS test. The ratios of the PSD at G_R to G_NR (blue dash line) and at FLY to G_NR (grey dash line) of each flight are given in each plot.

733

734
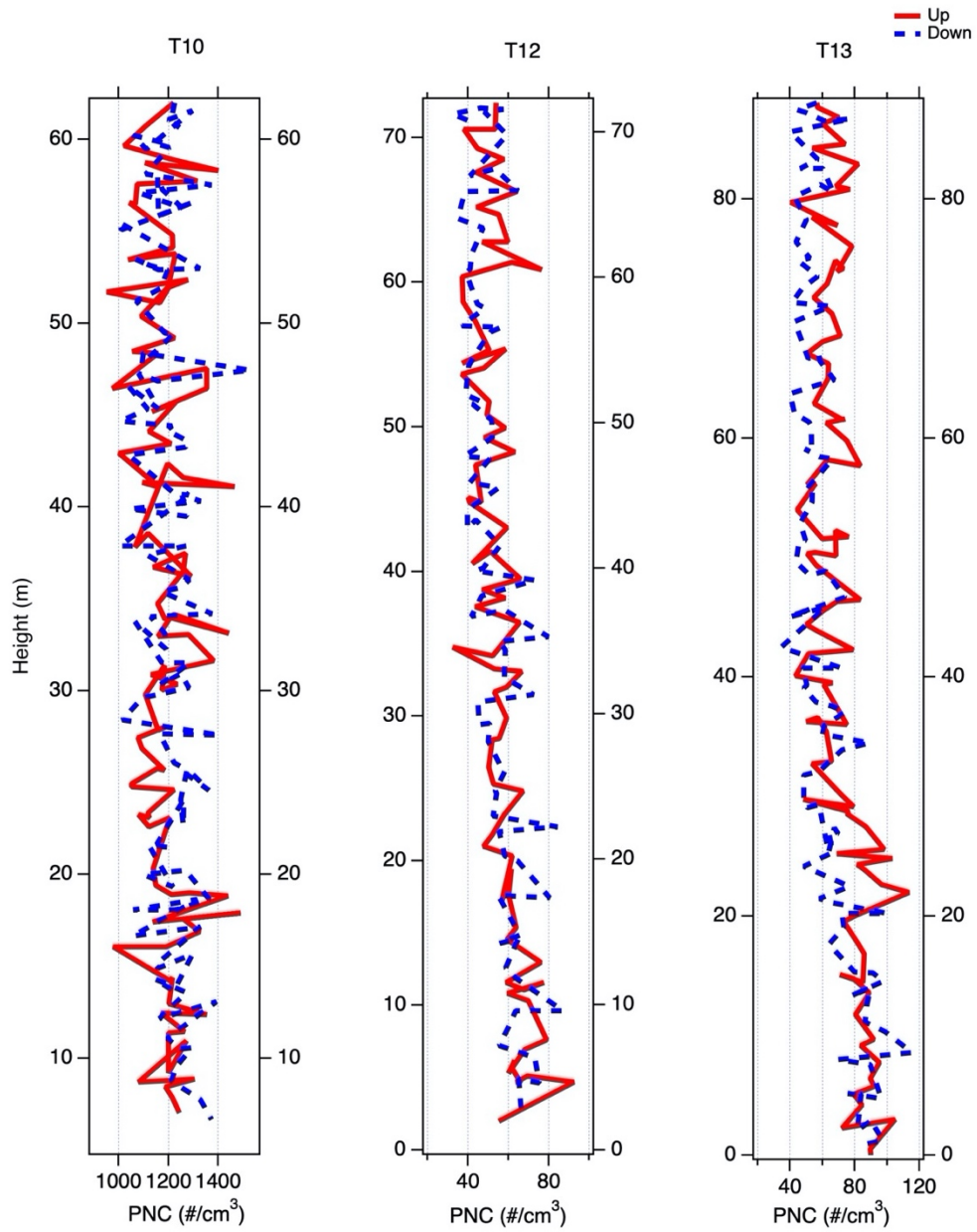
735
736 **Figure 6.** Vertical profiles of the particle number concentration in the profile runs of T10, T12,
737 and T13. The red line shows the observed concentration in the way up and the blue dash line
738 shows that in the way down, respectively.
739

740
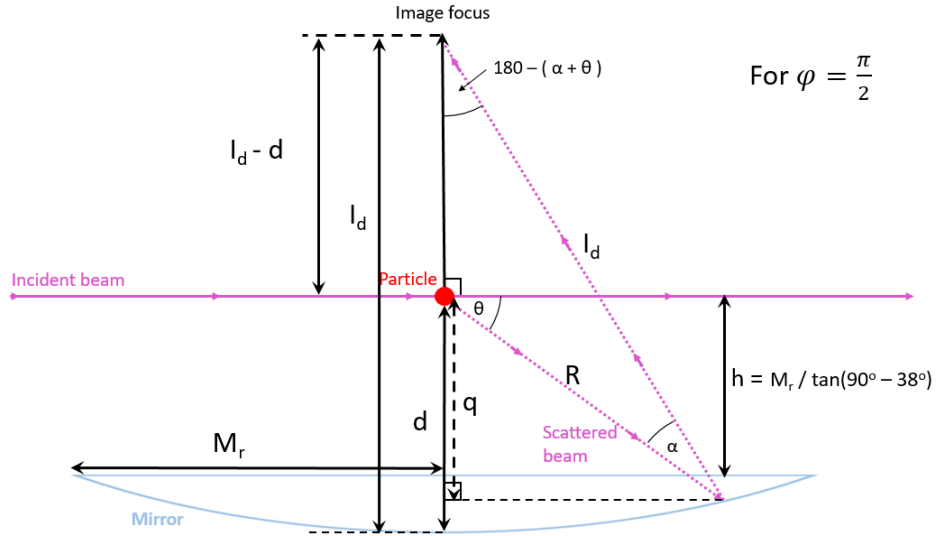
741 **Figure A1.** Geometry of POPS optical chamber. Values for the fixed parameters are listed in Table
742 A1.

743

744
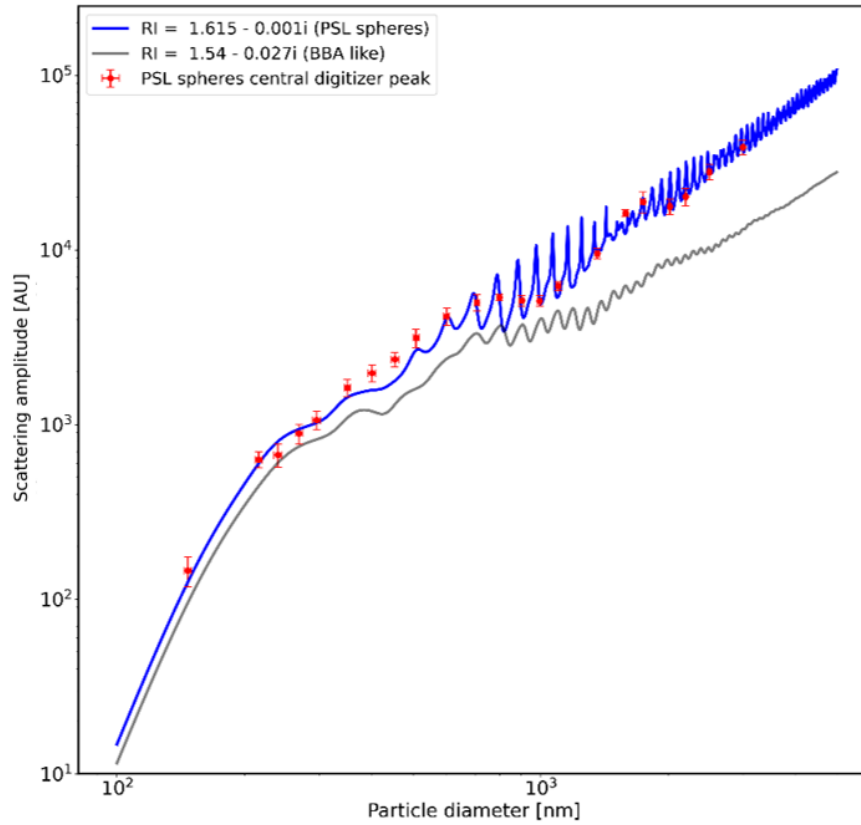
745 **Figure A2.** POPS scattering amplitudes for particles from 0.1μm to 4μm. Calculations for the blue
746 curve used the refractive index for PSL spheres and for the black curve a refractive index for biomass
747 burning particles. The red points are the real scattering amplitudes measured during the calibration
748 with PSL spheres. Both the blue and black curves have been scaled using the same scaling factor.
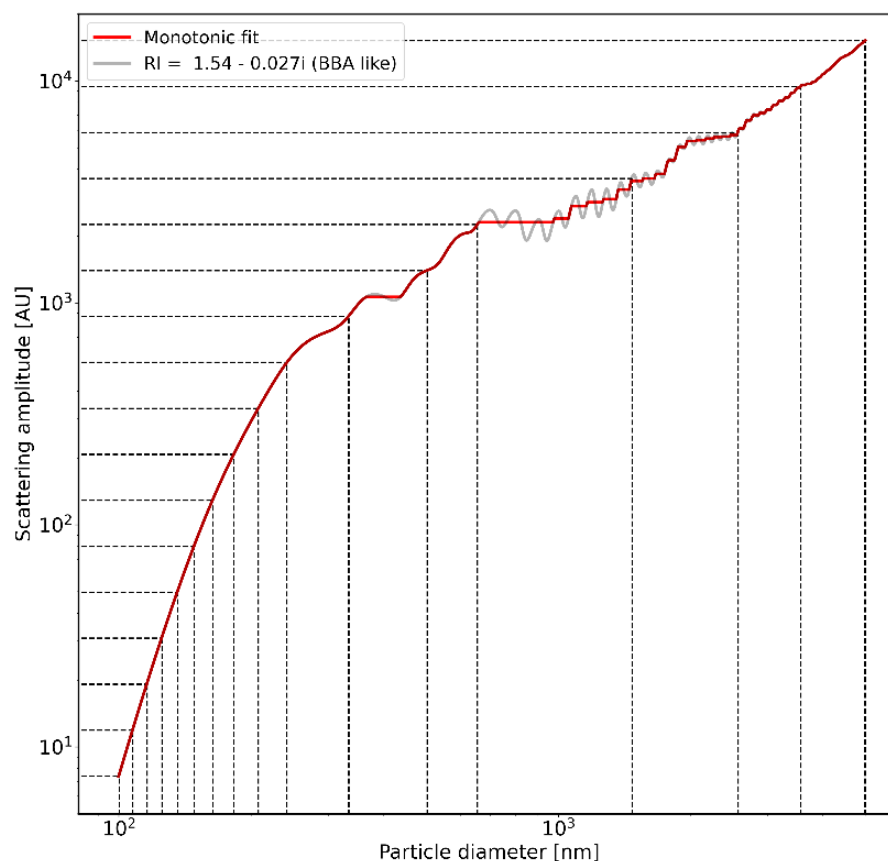
Figure A3. 16 bin boundaries logarithmically spaced in terms of peak value related to particle diameter using the scaled biomass burning curve from figure A2. The red line is a monotonically increasing fit.

	Date & Time	Time	Particle Number Concentrations (PNCs) (cm^{-3})			Percentage Difference (%)	
			G_NR	G_R	FLY	G_R	FLY
T1	18/Nov/2019	16:07-16:30	597±30	587±22	n/a	-1.7	n/a
T2	19/Nov/2019	17:00-17:35	741±52	767±35	742±31	3.5	0.1
T3	20/Nov/2019	14:20-15:10	442±48	479±23	478±40	8.4	8.1
T4	25/Nov/2019	10:36-11:15	317±36	349±21	385±30	10.1	21.5
T5	26/Nov/2019	15:21-16:00	207±19	228±18	230±31	10.1	11.1
T6	28/Nov/2019	11:08-11:46	567±50	580±30	561±41	2.3	-1.1
T7	2/Dec/2019	11:45-12:31	753±30	745±24	760±55	-1.1	0.9
T8	30/Jan/2020	11:49-12:34	22±4	24±5	36±11	9.1	63.6
T9	4/Feb/2020	10:41-11:15	87±11	91±11	105±19	4.6	20.7
T10*	7/Feb/2020	11:57-12:44	1063±29	1092±29	1169±84	2.7	9.9
T11	12/Feb/2020	16:35-17:26	156±16	181±13	187±21	16.0	19.9
T12*	26/Feb/2020	14:36-17:27	50±7	63±9	74±11	26	48
T13*	3/Mar/2020	11:24-12:06	79±10	86±13	102±13	8.9	29.1
T14	9/March/2020	11:55-12:28	95±12	90±10	108±14	-5.3	13.7

Table 1. Summary of the PNCs of each test flight at three stages. n/a = not applicable. The numbers denoted by ±x represent the standard deviation in the PNCs during the measurement time period.* indicates that profiles were also performed as documented here. T10: 5-60 m at 0.5 m s^{-1}; T12: 5-70 m at 1.0 m s^{-1}; T13: 2-90 m at 1.0 m s^{-1}.

	Surface Wind Speed (m/s)	T test P value	
		G_R	FLY
T1	0.5	0.2	n/a
T2	2.6	0.3	0.6
T3	5.7	2e-9	2e-7
T4	3.6	8e-5	2e-7
T5	6.7	2e-9	2e-6
T6	1.5	0.9	0.2
T7	1	0.9	0.3
T8	4.1	0.05	3e-6
T9	7.7	0.2	1e-10
T10	n/a	0.7	0.2
T11	n/a	2e-5	5e-6
T12	n/a	4e-10	1e-6
T13	n/a	0.02	1e-14
T14	n/a	0.2	1e-5

Table 2. Summary of the dates, time, wind speed, and t test results (p value) of each test flight. Wind speed values (at 1.5m) are the wind speed in the hour closest to the experiment time. From T10 to T14 the wind speed data is not available (n/a) because the instrument recording the data had broken. Flights highlighted in bold italic font indicate that the results are not significantly different at 5% significance. Flights marked in italic font indicate that the PNC on the ground with the rotor on are not significantly different from G_NR, and flights marked in standard font indicate that there are significant differences in both G_R and FLY when compared to G_NR.

	PNC RMSD (%)	
	G_R	FLY
All cases	10.2	26.2
Low wind speed cases (w<2.6m/s)	2.4	5
High wind speed cases (2.6<w<7.7m/s)	12.6	31.4
	PNC MAD (%)	
	G_R	FLY
All flights	7.8	19.1
Low wind speed cases (w<2.6m/s)	2.3	3
High wind speed cases (2.6<w<7.7m/s)	10.9	26.3

Table 3. Summary of RMSD and MAD for all cases, low wind cases, and high wind cases.

	Surface Wind Speed (m/s)	Sample flow rate (cm^3/s)		
		G_NR	G_R	FLY
T1	0.5	3.04±0.04	3.03±0.04	n/a
T2	2.6	3.04±0.04	3.04±0.05	3.03±0.12
T3	5.7	3.03±0.04	3.03±0.06	3.03±0.20
T4	3.6	3.04±0.04	3.03±0.05	3.03±0.16
T5	6.7	3.02±0.04	3.02±0.04	3.00±0.26
T6	1.5	3.02±0.04	3.03±0.04	3.03±0.15
T7	1	3.03±0.03	3.03±0.05	3.03±0.17
T8	4.1	3.03±0.03	3.03±0.04	2.99±0.28
T9	7.7	3.03±0.04	3.03±0.05	3.02±0.21
T10	n/a	3.02±0.04	3.02±0.04	3.03±0.19
T11	n/a	3.02±0.04	3.02±0.04	3.03±0.22
T12	n/a	3.02±0.03	3.02±0.04	3.04±0.16
T13	n/a	3.02±0.04	3.03±0.04	3.03±0.23
T14	n/a	3.02±0.04	3.02±0.05	3.00±0.17

Table 4. Summary of the sample flow rates of each test flight at three stages. n/a = not applicable. The numbers denoted by ±x represent the standard deviation in the sample flow rates during the measurement time period.

	Mean Percentage Difference (%)			
	G_R (%)		FLY (%)	
	Accumulation	Coarse	Accumulation	Coarse
T1	-2.1	17.5	n/a	n/a
T2	5.4	1.6	-0.7	-7.0
T3	10.8	67.4	9.7	17.5
T4	13.3	6.8	15.0	38.3
T5	7.7	19.5	6.4	35.6
T6	-0.8	22.0	-3.6	61.8
T7	-0.3	7.5	3.3	17.2
T8	11.6	83.0	53.2	123.1
T9	4.2	0.9	15.6	48.0
T10	4.9	19.8	14.9	42.4
T11	18.0	23.8	16.8	33.9
T12	25.2	23.0	43.2	14.8
T13	4.2	18.4	13.9	55.5
T14	-5.1	4.5	7.3	29.9
	RMSD (%)			
	G_R		FLY	
	Accumulation	Coarse	Accumulation	Coarse
All cases	10.6	32.2	21.6	49.5
Low wind speed cases (w<2.6m/s)	3.4	15.8	7.8	38.6
High wind speed cases (2.6<w<7.7m/s)	12.9	38.5	25.4	53.6
	MAD (%)			
	G_R		FLY	
	Accumulation	Coarse	Accumulation	Coarse
All cases	8.1	22.6	15.7	40.4
Low wind speed cases (w<2.6m/s)	2.7	13.7	5.6	32.1
High wind speed cases (2.6<w<7.7m/s)	11.1	27.5	20.1	44.1

Table 5. Summary of mean percentage differences of size distribution between G_NR and G_R, and G_NR and FLY of each flight. The size distributions are separated into two modes: accumulation mode ($0.1 \leq d \leq 1\mu m$) and coarse mode ($d > 1\mu m$).

	Mean PNCs (cm^{-3})	
	Up	Down
T10	1189±107	1201±101
T12	55±11	54±12
T13	72±15	82±13

849 **Table 6.** Mean PNC with standard deviations on the way up and down in three vertical profile
850 runs.

851
852
853
854
855
856
857
858
859
860

Parameter	Symbol	Approx. value
Focal length of mirror	fm	10mm
Distance from mirror to image	Id	33.3mm
Distance from beam to mirror	d	14.8m
Radius of mirror	Mr	12.5mm
Distance from beam to top of mirror	h	9.77mm

861 **Table A1.** Parameters derived from information in Gao et al. 2016